



City Research Online

City, University of London Institutional Repository

Citation: Yin, T., Ali, F. & Reyes-Aldasoro, C. C. (2015). A Robust and Artifact Resistant Algorithm of Ultrawideband Imaging System for Breast Cancer Detection.. IEEE Trans Biomed Eng, 62(6), pp. 1514-1525. doi: 10.1109/tbme.2015.2393256

This is the accepted version of the paper.

This version of the publication may differ from the final published version.

Permanent repository link: <https://openaccess.city.ac.uk/id/eprint/8364/>

Link to published version: <https://doi.org/10.1109/tbme.2015.2393256>

Copyright: City Research Online aims to make research outputs of City, University of London available to a wider audience. Copyright and Moral Rights remain with the author(s) and/or copyright holders. URLs from City Research Online may be freely distributed and linked to.

Reuse: Copies of full items can be used for personal research or study, educational, or not-for-profit purposes without prior permission or charge. Provided that the authors, title and full bibliographic details are credited, a hyperlink and/or URL is given for the original metadata page and the content is not changed in any way.

City Research Online:

<http://openaccess.city.ac.uk/>

publications@city.ac.uk

A Robust and Artifact Resistant Algorithm of Ultrawideband Imaging System for Breast Cancer Detection

Tengfei Yin, *Student Member, IEEE*, Falah H. Ali*, *Senior Member, IEEE*, and Constantino Carlos Reyes-Aldasoro, *Senior Member, IEEE*

Abstract—Goal: Ultrawideband radar imaging is regarded as one of the most promising alternatives for breast cancer detection. A range of algorithms reported in literature show satisfactory tumor detection capabilities. However, most of algorithms suffer significant deterioration or even fail when the early-stage artifact, including incident signals and skin-fat interface reflections, cannot be perfectly removed from received signals. Furthermore, fibro-glandular tissue poses another challenge for tumor detection, due to the small dielectric contrast between glandular and cancerous tissues. **Methods:** This paper introduces a novel Robust and Artifact Resistant (RAR) algorithm, in which a neighborhood pairwise correlation-based weighting is designed to overcome the adverse effects from both artifact and glandular tissues. In RAR, backscattered signals are time-shifted, summed, and weighted by the maximum combination of the neighboring pairwise correlation coefficients between shifted signals, forming the intensity of each point within an imaging area. **Results:** The effectiveness was investigated using 3-D anatomically and dielectrically accurate finite-difference-time-domain numerical breast models. The use of neighborhood pairwise correlation provided robustness against artifact, and enabled the detection of multiple scatterers. RAR is compared with four well-known algorithms: delay-and-sum, delay-multiply-and-sum, modified-weighted-delay-and-sum, and filtered-delay-and-sum. **Conclusion:** It has shown that RAR exhibits improved identification capability, robust artifact resistance, and high detectability over its counterparts in most scenarios considered, while maintaining computational efficiency. Simulated tumors in both homogeneous and heterogenous, from mildly to moderately dense breast phantoms, combining an entropy-based artifact removal algorithm, were successfully identified and localized. **Significance:** These results show the strong potential of RAR for breast cancer screening.

Index Terms—Breast cancer detection, delay-and-sum (DAS), finite-difference time-domain (FDTD), ultrawideband (UWB) imaging.

I. INTRODUCTION

BREAST cancer is the most common cancer among females [1], and one of the leading causes of death worldwide [2]. Although less common in males, detected incidences of breast cancer among males have been increasing

This work was supported by the China Scholarship Council (CSC) and the University of Sussex Joint Scholarships.

Tengfei Yin and *Falah H. Ali are with Communications Research Group, School of Engineering and Informatics, University of Sussex, Brighton, BN1 9QT, UK. (correspondence e-mail: f.h.ali@sussex.ac.uk).

Constantino Carlos Reyes-Aldasoro is at City University London, Northampton Square London, EC1V 0HB, UK.

recently [3]. Early diagnosis of breast cancer is one of the most challenging and important aspects for the management of the disease, as it may be possible to detect the cancer before it spreads [4]. Three commonly used screening methods for breast cancer are X-ray mammography [5], Ultrasound (US) [6], and Magnetic Resonance Imaging (MRI) [7]. A higher rate of false-positive examination results with US makes it less popular than mammography [8], whereas MRI is usually suggested to be used in conjunction with mammography [9]. Despite the merits of mammography, its deficiencies are evident: low sensitivity [10], painful breast compression [11], and radiation exposure from X-rays, which brings a potential threat of increasing the cancer risk [12]. The limitations of existing methods constitute a motivation for better options.

In the last few decades, different modalities of microwave imaging for breast cancer detection, including passive, hybrid, and active approaches, have attracted considerable attention. The passive imaging techniques seek to identify tumors based on the temperature differences between normal and cancerous breast tissues with the aid of radiometers [13]-[14]. Hybrid approaches differentiate biological tissues by the distinctive acoustic waves radiated from the thermoelastic expansion when tissues are under microwave illumination [15]. Active methods distinguish normal and malignant breast tissues based on their contrast of dielectric properties at microwave frequencies [16]. Based on the reconstruction technique used, active detection methods can be categorized into microwave tomography and ultrawideband (UWB) radar based imaging. In microwave tomography, the spatial distributions of dielectric constant and/or conductivity within the breast are iteratively calculated, thus nonlinear inverse scattering problems are involved. More details on tomographic imaging systems can be found in [17], [18]. UWB radar methods, on the other hand, aim to identify the presence and location of strong scatterers such as tumors, rather than quantitatively computing the distribution of dielectric properties.

UWB radar based imaging systems face several challenges for breast cancer detection, two of them is the antenna design, and the construction of realistic finite-difference time-domain (FDTD)-based [19] breast model. Another difficult challenge is image formation algorithm. The image formation algorithm is expected to provide superior tumor identification ability, accurate positioning, strong robustness, and fast computation speed. A variety of image formation algorithms have been

proposed over the last decade. Hagness *et al.* [20]-[21] first proposed the confocal microwave imaging (CMI) technique which adopted delay-and-sum (DAS) beamforming algorithm. Research on beamforming algorithms for CMI has evolved into two branches: data-dependent and data-independent. Some promising data-dependent beamforming algorithms that have been considered are multistatic adaptive microwave imaging (MAMI) [22], multi-input multi-output (MIMO) [23], and time-reversal multiple signal classification (TR-MUSIC) [24]-[25]. Data-dependent algorithms can reconstruct high-resolution images when the array steering vector corresponding to the signal of interest (SOI) is accurately known, which is difficult in realistic breast imaging scenarios. In contrast, data-independent beamformers are free from this prior information and have been constantly developed. A number of data-independent algorithms are proposed in recent years, including delay-multiply-and-sum (DMAS) [26], modified-weighted-delay-and-sum (MWDAS) [27], and filtered delay-and-sum (FDAS) [28]-[29]. Compared with the classical DAS algorithm, improved performance of clutter rejection is offered by DMAS and MWDAS. FDAS shows its capability of detecting multiple scatterers in dense breasts, where the presence of fibro-glandular tissue is considered. It is recognized that the increased heterogeneity of normal breasts introduced by glandular tissues constitutes a big challenge for tumor detection. There are two reasons for this: first, although there is a large dielectric contrast between adipose and cancerous tissues, the difference between glandular and cancerous tissues is much less pronounced. Also the glandular tissue introduces a significant amount of attenuation and dispersion in backscattered signals, making it more difficult to detect any small tumors present. Despite the strengths of these algorithms, all of them are only examined in scenarios assuming an ideal artifact removal method is applied. However, this assumption is oversimplified and infeasible in a real set-up. Because the artifact is typically several orders of magnitude greater than the reflections from tumors within the breast, even a very small amount of residual artifact can easily mask the desired tumor response, which may result in the failure of existing algorithms to identify any tumors present.

In this paper, a new Robust and Artifact Resistant (RAR) image formation algorithm for early breast cancer detection is proposed. Extensive simulations and analyses using backscattered signals received from three-dimensional (3-D) anatomically realistic MRI-derived numerical breast models were conducted to validate the performance of the proposed algorithm. Results showed that RAR offered superior tumor identification, accurate localization, and strong artifact resistance over existing data-independent algorithms. The robustness of RAR was demonstrated under various scenarios: homogenous and heterogeneous breast models with varied densities, combining both ideal and practical artifact removal methods were considered. The remainder of this paper is organized as follows: in Section II, the breast model and the configuration of imaging system are introduced. Section III presents the RAR algorithm and Section IV describes the

assessment criteria of algorithms and corresponding results. Concluding remarks are summarized in Section V.

II. BACKSCATTERED SIGNAL ACQUISITION

A. Breast Model

Realistic models must incorporate various attributes of the breast, including geometrical properties, spatial distribution of different constituent tissues, and the dispersive property. In this study, 3-D anatomically accurate FDTD-based breast models are developed and employed, based on UWCEM MRI breast cancer repository [30]. Besides skin layer and malignant tumor, the breast model comprises three types of fatty and three types of fibro-glandular tissues. The dielectric properties of skin, fatty, and glandular tissues used in the model are based on Lazebnik's studies [31], whereas those representing malignant tumors are obtained from Bond *et al.* [32].

The dispersive nature of tissues is incorporated into the FDTD model using the time-domain auxiliary differential equations (ADE) ([19], Ch. 9) for a single-pole Debye model. In a Debye model, the dielectric spectrum of a tissue sample is characterized by different dispersive regions or 'poles' at a range of frequencies. In each dispersive region there is a relaxation time, which describes the time needed for electron polarization to relax towards a new equilibrium when there is an applied electric field. The relaxation time is regarded as a constant in the simplest form. The dispersion in frequency domain through Debye model can be described as [33]:

$$\epsilon_r(\omega) = \epsilon_\infty + \sigma_s/j\omega\epsilon_0 + (\epsilon_{s1} - \epsilon_\infty)/(1 + j\omega\tau_1) \quad (1)$$

where $\epsilon_r(\omega)$ is the calculated relative permittivity at a certain frequency, ϵ_∞ is the permittivity in infinite frequency, σ_s is the static conductivity (in siemens per second), ϵ_0 is the free-space permittivity (8.854 pF/m), ϵ_{s1} is the permittivity at static frequency of the dispersive pole, $j = \sqrt{-1}$, ω is the angular frequency (in radians per second), $\omega = 2\pi f$, f (in Hz) is the frequency of input signal, and τ_1 is the relaxation time of the dispersive pole (in picoseconds). Debye parameters for each tissue type are summarized in Table I [34].

TABLE I
TISSUE PARAMETERS ASSUMED FOR THE SINGLE-POLE DEBYE MODEL

	ϵ_∞	ϵ_{s1}	τ_1 (ps)	σ_s (S/m)
Fat-High	3.9870	7.5318	13.0000	0.0803
Fat-Median	3.1161	4.7077	13.0000	0.0496
Fat-Low	2.8480	3.9521	13.0000	0.2514
Fibro-glandular High	14.2770	54.7922	13.0000	0.6381
Fibro-glandular Median	13.8053	49.351	13.0000	0.7384
Fibro-glandular Low	12.8485	37.4915	13.0000	0.2514
Skin	15.9300	39.7600	13.0000	0.8310
Malignant Tumor	20.2800	45.5000	13.0000	1.3000

Fig. 1 illustrates the 3-D breast phantom and antenna configuration used in our simulation. To focus on the breast tissue response and avoid possible interference, the chest wall is not included as assumed in [25] and [28]. Two concentric rings of antennas are positioned around the skin layer, which

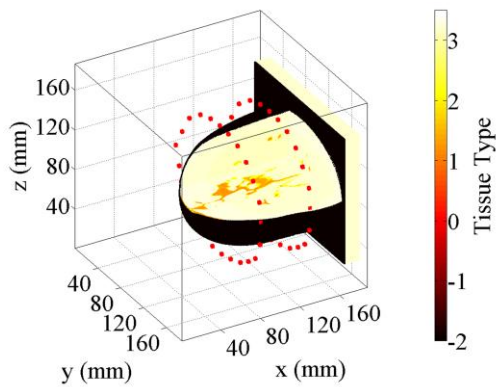


Fig. 1. 3-D FDTD breast model with two concentric rings of 24 antennas (indicated by solid dots) surrounding the breast. The different tissue types are represented by difference values: fat-high(3.1), fat-median(3.2), fat-low(3.3), fibro-glandular (FG)-high(1.1), FG-median(1.2), FG-low(1.3), and skin(-2).

has a thickness of 1.5 mm, with a 10 mm spacing to the skin surface. Each element is modeled as a point source with horizontal polarizations (x -directed). The outer ring of antennas is at $x = 80$ mm (antennas 1 to 24), and the inner ring (antennas 25 to 48) is at $x = 130$ mm, in which the position of both rings are related to the chest wall. The same yz plane coordinates for both rings of antennas are: (39, 101), (50, 120), (63, 140), (82, 153), (100, 158), (116, 159), (131, 158), (147, 154), (162, 145), (174, 132), (185, 116), (192, 97), (189, 74), (178, 56), (166, 47), (152, 39), (135, 34), (119, 32), (103, 31), (84, 38), (71, 44), (59, 55), (43, 69), and (37, 83).

For completeness, six breast medium types with various structures and radiographic density classifications are evaluated with the proposed algorithm. The medium types are selected from the UWCEM database [30] and shown in Fig. 2. The density follows the definitions of the American College of Radiology (ACR) [35]. The details of these phantoms are the following (ACR type, Breast ID, characteristics): a) medium type A: ACR-I-ID-071904, homogenous breasts composed of fatty-median tissue only, all other tissues are replaced by the fatty-median tissue; b) medium type B: ACR-I-ID-071904, heterogeneous breasts composed of three types of fatty tissues, all glandular tissues are replaced by the fatty-median tissue; c) medium type C: ACR-I-ID-071904, full heterogeneous breasts composed of three types of fatty, and three types of glandular tissues with a percentage less than 25%; d) medium type D: ACR-II-ID-010204, full heterogeneous breasts contain glandular tissues with a percentage ranging between 25% and 50%; e) medium type E: ACR-III-ID-070604PA2, full heterogeneous breasts contain glandular tissues with a percentage ranging between 50% and 75%; f) medium type F: ACR-IV-ID-012304, full heterogeneous breasts contain glandular tissues with a percentage over 75%.

Although tumors have irregular shapes, for this study they are constructed as spheres. Without losing generality, a 10 mm diameter tumor is placed at three different positions are considered: 1) close to the center of the outer ring; 2) at the center between the two antenna rings; and 3) off-center between the two antenna rings. Position 1 at $(x, y, z) = (80, 119, 94)$ represents tumor locations on different x cross-sections and are close to one of the antenna rings. Position 2 at

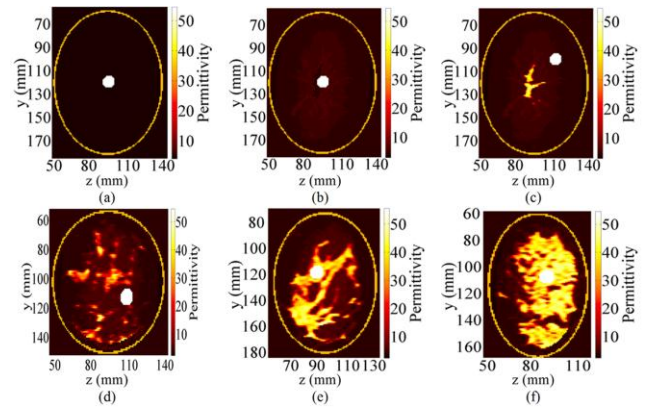


Fig. 2. Breast medium types represented by relative permittivity at center frequency of input pulse [30]. A tumor with 10 mm diameter is constructed as a sphere. The 2D slices are taken at the x cross-sections of Fig. 1.

$(x, y, z) = (95, 119, 94)$ is representative for those which are between two antenna rings and center at the yz plane with different x cross-sections. Those off-center at the yz plane with different x cross-sections and are close to the skin surface are represented by Position 3 at $(x, y, z) = (95, 99, 112)$. In addition, since a high proportion of breast cancers are invasive ductal carcinomas, which start at fibro-glandular regions [36], tumors which are located within fatty and glandular tissues are both considered. To avoid the strong reflections from skin-fat interface, the entire model and antenna array are considered to be positioned inside an immersive liquid with the same permittivity as that of fat-median tissue at the center frequency of the input pulse, as it is generally done [26], [27].

B. Measurement Setup

The antenna array is excited with a modulated Gaussian pulse (Fig. 3), which is given by

$$G(t) = \sin[\omega_c(t - b)] \exp\{-[(t - b)/c]^2\} \quad (2)$$

where $\omega_c = 2\pi f_c$ is the center angular frequency with $f_c = 6.85$ GHz, the center position of Gaussian envelope $b = 0.375$ (ns), and $c = 0.0802$ (ns) is the standard deviation which controls the width of Gaussian envelope. Gaussian modulated pulses are selected since they are considered to present better spectral control in practical use [37]. The input pulse width is 0.56 (ns), which has a full-width at half maximum (FWHM) bandwidth of 6.6 GHz. The acquisition of backscattered signals can be implemented by monostatic or multistatic method. In the monostatic approach, each element in the antenna array transmits the pulse and receives backscattered signals from the breast model sequentially. In the multistatic method, each element in the antenna array takes a turn to transmit and the backscattered signals are recorded at all elements. Despite the advantage of multistatic approach in terms of capturing more information about the target, its disadvantages are obvious, such as additional hardware cost and high algorithmic complexity. Monostatic method is adopted for data acquisition in this study. To discretize the FDTD problem space, a rule of thumb to select the grid size is to keep it below one-tenth of the wavelength, with the purpose

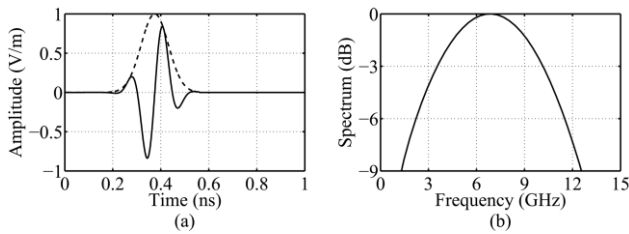


Fig. 3. Modulated Gaussian pulse used as the UWB excitation signal in the FDTD breast model simulations. (a) Time domain. (b) Frequency domain.

of making numerical dispersion error negligible [38]. Assuming the breast is mainly composed of fatty-median tissue, and using the center frequency of input pulse as a baseline, obtaining the wavelength is 21 mm, thus one-tenth of wavelength is 2.1 mm. A smaller grid size of $\Delta x = \Delta y = \Delta z = 1$ mm is employed for capturing the response from small sized tumors and adapting possible smaller wavelengths in dense breasts. The time step represented by Δt is determined by the Courant-Friedrich-Lecy (CFL) stability condition [19], which equals 1.91 (ps) in our simulation. Ten-layer convolutional perfectly matched layer (CPML) [39] absorbing boundary conditions are placed around the computational domain to attenuate outgoing radiation.

III. IMAGE RECONSTRUCTION

A. Pre-processing for Artifact Removal

Recorded backscattered signals consist of two parts: the early-stage and the late-stage. The majority of early-stage parts consist of incident signals and strong reflections from skin-fat interface, whereas the late-stage parts include tumor response, glandular tissue response, fatty tissue response, and the multi-reflections between these tissues. Tumor, glandular, and fatty responses refer to the signals directly reflected from these tissues. For identification, only tumor response is needed, and all other signals are viewed as interference, which can be categorized as the early-stage artifact and the late-stage clutter. The late-stage clutter mainly includes glandular and fatty tissues responses, which mix with tumor response and should be suppressed for effective tumor detection. The early-stage artifact includes incident signals and skin-fat reflections. The incident signal refers to the transmitted signal being received directly (non-reflected) at the same transmitting antenna. These artifact can be several orders of magnitude greater than the desired tumor response, thus they must be removed before applying any image reconstruction algorithms.

Ideal removal of the early-stage artifact is realized with the aid of a *priori* information generated from a tumor free breast model. The ideal tumor response from the i th transceiver in a discrete form denoted as $S_i(n)$ can be obtained by

$$S_i(n) = S_{i_with_tumor}(n) - S_{i_tumor_free}(n) \quad (3)$$

where $n = 1, 2, \dots, K$, and K is the signal sampling number, $S_{i_with_tumor}(n)$ is the backscattered signal received at the i th transceiver from a breast with tumor, and $S_{i_tumor_free}(n)$ represents the backscattered signal received at the same

transceiver from a breast which is exactly the same as the previous one except that no tumor present. $S_{i_with_tumor}(n)$ is composed of early-stage artifact, tumor response, glandular tissue response, fatty tissue response, and the multi-reflections between different tissues, while $S_{i_tumor_free}(n)$ comprises similar level of early-stage artifact, glandular tissue response, fatty tissues response, and multi-reflections between them, thus $S_i(n)$ is the signal dominated by tumor response. This method not only removes the early-stage artifact, but also the glandular tissue response, fatty tissue response, and the multi-reflections between tissues. This is not feasible in practice; however, it could serve as a useful benchmark of the best performance of algorithms possible. A number of more practical artifact removal algorithms have been developed, these can be classified as adaptive and non-adaptive techniques. Adaptive methods include Wiener filter [32], recursive least squares (RLS) filter [40], and singular value composition (SVD) [41], whereas some other promising techniques include average subtraction [20], rotation subtraction [42], frequency domain pole splitting [43], and entropy-based time window [44]. Robustness to local variations of skin thickness and differences in antenna-skin distances are observed in adaptive filtering methods, however, varied levels of distortion to the tumor response is introduced. Considering both the capability of preserving tumor response and the effectiveness of removing artifact, the best results are offered by Wiener filter and entropy-based time window [45].

The performance of beamformers closely depends on the outcome of artifact removal. If artifact cannot be removed effectively, the residual artifact could easily mask the tumor response. For completeness and fairness, it is thus essential to evaluate all beamformers in various cases with both ideal and non-ideal artifact removal, under the same conditions.

B. RAR Algorithm

The block diagram in Fig. 4 shows RAR to reconstruct the intensity value of each pixel in breast model. Let l represent the l th location of a pixel within the imaging area L . For each location, RAR explores and exploits the correlation between time-shifted signals. To time-shift each signal, an estimated average velocity for all propagation channels, between transmitter to scatterer and back to receiver, is assumed to be sufficiently close to the actual speed and could well represent the characteristics of propagation channels. Higher correlation between time-shifted signals at neighboring antenna pairs is more likely to occur at tumor positions. Considering the larger dielectric property of tumor than other comparably sized tissues, tumor response is the dominant part of received signals within a certain time window, in most if not all cases. Thus, time-shifted signals should have a higher correlation between tumor responses resulted from the same strong scatterer, compared with those signals from other heterogeneous breast tissues. The enhancement of tumor detection is achieved by rewarding this correlation. To calculate the intensity value of l , three steps are involved.

Step 1. Each pre-processed $S_i(n)$ is time-shifted based on the corresponding round-trip time delay at l . The time-shifted

signals are expressed as $S_i(n + \tau_{il})$, where $n = 1, 2, \dots, K$, and τ_{il} is the two-way travel time from the i th transceiver to a specific location l within the imaging region. Propagation distance is calculated based on space coordinates in the model. Signal propagation speed is calculated under the assumption that each traversed medium, including immersive liquid, skin layer, and underlying breast tissue, has a constant relative permittivity at the center frequency of input pulse. The relative permittivity at center frequency is chosen because it represents the majority of tissues' permittivity across the frequency range of the input pulse. The average dielectric property of underlying breast tissue is assumed to be established through an appropriate patient-specific dielectric properties estimation algorithm such as the one developed by Winters *et al.* [46].

Prior to further processing, a window truncation for each time-shifted signal is applied. The utility of time window truncation is twofold. First, it only preserves the desired tumor response. Second, it reduces the algorithmic complexity since only truncated signals are needed in the following steps. The time window is represented as W_α , where $W_\alpha = \alpha \Delta t$. α is an integer and Δt is the time step used in FDTD, which equals 1.91 (ps) as explained in Section II B. W_{294} which represents a length $294\Delta t = 562$ (ps), equals to the input pulse is used as a default time window, unless otherwise specified. The selection of this length is because backscattered signals from dispersive biological tissues are a distorted version of the excitation pulse as frequency-dependent tissues broaden the duration of the input pulse. Studies show that this broadening effect is directly proportional to the tumor size [32]. The aim of this research is to detect early-stage breast cancer when the tumor size is small, thus a short-length time window, which is comparable to the input pulse width, is selected. Larger or smaller time windows could result in either high clutter or tumor location bias. Thus, the time-shifted signal after truncation with length of W_α can be represented as $S_i(n + \tau_{il})$, where $n = 1, 2, \dots, \alpha$.

Let A be the number of antennas. After artifact removal, A calibrated signals containing tumor responses are collected in a monostatic way. Thus, for every single location l , there are A sets of time delays corresponding to each transceiver. Let $Sum_l(n)$ ($n = 1, 2, \dots, \alpha$) denote the sum of all time-shifted signals within the time window W_α at l given by

$$Sum_l(n) = \sum_{i=1}^A S_i(n + \tau_{il}) \quad (4)$$

Step 2. To enhance tumor response, and eliminate the adverse effects resulted from both the early-stage artifact and the late-stage clutter, a weight factor wf_l for the l th location is introduced. The Pearson's correlation coefficient $r_{ij,l}$ between neighboring pair of time-shifted signals is calculated as

$$r_{ij,l} = \frac{\sum_{n=1}^{\alpha} X_i(n)X_j(n)}{\sqrt{\sum_{n=1}^{\alpha} X_i(n)^2 \sum_{n=1}^{\alpha} X_j(n)^2}} \quad (5)$$

where $X_i(n) = S_i(n + \tau_{il})$ and $X_j(n) = S_j(n + \tau_{jl})$ with $j = i + 1$, are the time-shifted signals at l from the i th and $(i + 1)$ th transceiver, respectively. $r_{ij,l}$ measures the degree of coherence between time-shifted signals. High positive

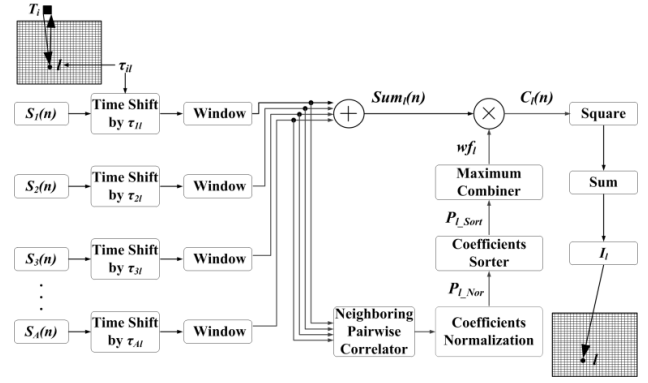


Fig. 4. Block diagram illustrating the RAR algorithm used to calculate the intensity of the l th pixel I_l in the imaging region indicated by the mesh area.

correlation between signals received from neighboring antenna pairs is expected at tumor locations, considering all time-shifted signals are a broadened version of the same input pulse, after reflect from the same strong scatterer. Based on (5), the neighborhood pairwise correlation coefficients vector P_l composed of $(A - 1)$ elements for l is obtained, where A is the number of antenna. Thus, P_l can be expressed as

$$P_l = [r_{12,l} \ r_{23,l} \ \dots \ r_{(A-1)A,l}] \quad (6)$$

Considering correlation coefficient $r_{ij,l}$ is in the range of $[-1, 1]$, all coefficients are linearly normalized to the range of $[0, 1]$, avoiding negative coefficients generating a high weight.

$$P_{l,Nor} = (P_l + 1)/2 \quad (7)$$

Let $P_{l,Sort}$ be the sorted $P_{l,Nor}$ in a descending order and $R_{i,l}$ be the sorted coefficients, $i = 1, 2, \dots, (A - 1)$. Therefore,

$$P_{l,Sort} = [R_{1,l} \ R_{2,l} \ \dots \ R_{(A-1),l}] \quad (8)$$

where $R_{1,l} > R_{2,l} > \dots > R_{(A-1),l}$. The associated weighting factor wf_l for the l th location is introduced as

$$wf_l = \prod_{i=1}^{(A-1)/2} R_{i,l} \quad (9)$$

which is the product of the first half elements of $P_{l,Sort}$. The neighborhood pairwise correlation ensures that the correlation between two antennas for each location is measuring the reflection from the same scatterer, because of the short distance between two neighboring antennas. The distance between adjacent array element of 20 ± 5 mm is used since it provided an optimum trade-off between performance and complexity. Considering the useful tumor response contained in signals from different antennas varies, depending on tumor locations, skin thickness variations, differences in antenna-skin distances, and interfering responses from other tissues, the selective multiplication of the maximum half coefficients is adopted. This mechanism implements the adaptive combination of antenna pairs, which guarantees the introduced weight can focus on those strongest scatterers, regardless of tumor's position. Considering malignant tumors' higher

scattering cross-section relative to comparably sized heterogeneity in normal breast tissue [32], wf_l adaptively rewards potential tumor locations with a high weight, thereby enhancing tumor identification in most if not all cases.

Step 3. The last step calculates the intensity for the l th location. Although the maxima of coherent addition of time-aligned signals may no longer exactly correspond to the tumor location in a complex medium, the sum still has a relatively high value at tumor locations, since signals from some, if not all antennas, are still able to add coherently. The constructed signal $C_l(n)$ in the RAR algorithm is therefore

$$C_l(n) = wf_l \cdot Sum_l(n) \quad (10)$$

Let I_l denote the intensity of a specific location l within the desired imaging area, and it is given by

$$I_l = \sum_{n=1}^{\alpha} [C_l(n)]^2 \quad (11)$$

The procedure is repeated for every location within the imaging region as shown in Fig. 4, and L loops in total are required. The distribution of intensity at each location I_l is displayed as an image. The pairwise correlation in the proposed RAR algorithm measures the backscattered energy intensity from each scatterer. The combination of neighboring antennas ensures that the strong reflection received at each neighborhood antenna pair is from the same strong scatterer, considering possible multi-scatterer cases. The maximum combining of correlation coefficients implements an adaptive selection of neighborhood paired antennas, only those that have a high correlation can contribute to the weight factor, yielding a flexible beamforming. The efficacy and robustness of RAR are demonstrated under a variety of challenging scenarios, where non-perfect artifact removal, and in breasts with varied levels of glandular tissues are considered, and these are presented in the following sections.

IV. PERFORMANCE ANALYSIS

In this section, algorithm performance is analyzed in depth. The superiority of RAR is demonstrated via comparisons with four techniques, including DAS, DMAS, MWDAS, and FDAS. First, algorithms were evaluated in mostly sparse breasts with medium type A and B, applying an idealized artifact removal method. Then combining practical artifact removal methods, the algorithm effectiveness was investigated for dense breast models with various medium compositions and tumor positions. The computational analysis of algorithms is also provided considering its significance in practical use.

A. Ideal Artifact Removal

Serving as a benchmark of imaging algorithm performance, ideal artifact removal (Fig. 5) for obtaining clear tumor response was firstly applied. It can be seen that desired tumor response indicated by the dotted box in Fig. 5(c), which exists in later time, is totally obscured in received signals in Fig. 5(a). This is due to its small order of magnitude, compared with that of incident signals and skin reflections appear earlier.

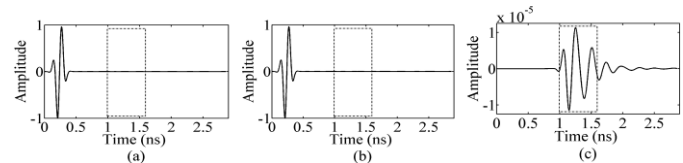


Fig. 5. Illustration of ideal artifact removal. (a) Signal recorded at antenna 4 of Fig. 1. A tumor with a 10 mm diameter is placed at $(x, y, z) = (95, 99, 112)$. (b) Signal recorded from a tumor-free breast model. (c) Pure tumor response obtained by subtracting (b) from (a), which is indicated by dotted boxes.

All reconstructed images were normalized to the maximum intensity value of the 3-D imaging volume. Same datasets were applied for all algorithms. To assess algorithm's imaging performance, two quantitative metrics were applied, which are signal-to-clutter ratio (SCR) and signal-to-mean ratio (SMR). SCR was defined as the ratio of the maximum tumor response to the maximum clutter response, whereas SMR was defined as the ratio of mean tumor response to the mean response of the whole image. The maximum or mean tumor response was assumed to be the peak or average intensity of an area defined by twice physical extent of the tumor [26], whereas clutter response was those outside this area. SCR defines the difference between tumor and clutter response, whereas SMR shows the image contrast between tumor and non-tumor areas.

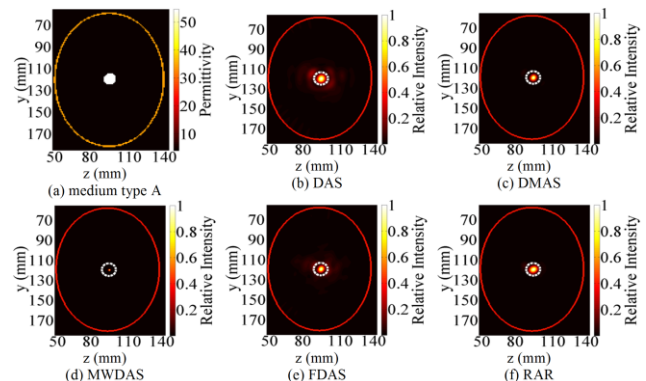


Fig. 6. (a) 2D slice of breast model of medium type A. (b)-(f) Imaging results with ideal artifact removal. Tumor's position is indicated by dotted circle.

Fig. 6 presents the reconstructed images through the five techniques, representing a distribution of energy resulted from each voxel within the breast model. The peak intensity of image is usually regarded as the tumor position, which has the strongest reflection among all heterogeneous breast tissues with a comparable size [32]. It can be seen that the embedded 10 mm diameter tumor is clearly identified and accurately localized by all algorithms. However, the clutter rejection capability of them varies due to the different weighting mechanisms employed. Specifically, the image offered by DAS [Fig. 6(b)] is filled with the strongest level of clutter, which is indicated by the smallest SCR of 7.01 dB (Table II). This shows its limited capability for discriminating against clutter since it does not account for any dispersive propagation effect. The result of FDAS [Fig. 6(e)] is cleaner than that of DAS, which validates the effectiveness of its filtering process, but its performance is still inferior to the other three algorithms. It is observed that DMAS, MWDAS, and the proposed RAR algorithm provided almost clutter-free images

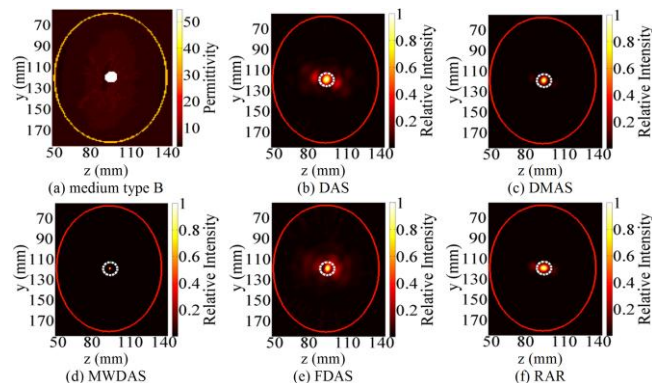


Fig. 7. (a) 2D slice of breast model with medium type B. (b)-(f) Imaging results with ideal artifact removal.

[Fig. 6(c), (d), and (f)]. Assuming perfect tumor response could be captured, the cross multiplying of weighted tumor response from all channels in MWDAS forms particularly high weights [Fig. 6(d)], which achieved the strongest clutter rejection with a SCR of 415.58 dB in this case.

Imaging results in Fig. 7 employ the same ideal artifact removal method as in Fig. 6, but the breast model is changed from homogeneous fatty to heterogeneous fatty [Fig. 7(a)], in which three different fatty tissues, fatty-low, fatty-median, and fatty-high are included. With increased heterogeneity, more dispersion of received signals is expected due to the increased propagation behavior difference of frequency components among various tissues. Furthermore, the estimated average propagation velocity might not as well represent the actual speed as in the homogeneous case, leading to a mismatch between the estimated and actual time delay. This is reflected by the imaging results. Compared Fig. 6(b) with Fig. 7(b), both of which are the results of DAS, more clutter outside the circle is observed in Fig. 7(b), corresponding to a 2.03 dB decrease of SCR. The same trend applies for all algorithms considered. Despite a slight degradation of clutter suppression, the inserted tumor is accurately localized by all techniques. This also indicates the fault-tolerant capability of these algorithms for certain propagation time-delay mismatch.

B. Realistic Artifact Removal

Previous results show that all algorithms present decent tumor identification and localization capabilities, regardless of homogeneous or heterogeneous breasts, assuming the tumor response could be ideally extracted. However, perfect removal of artifact is unlikely in practice, it is therefore critical to test algorithms' performance in scenarios applying more realistic artifact removal methods. The artifact is a mixed signal composed of incident signals and skin-fat interface reflections, thus pure tumor response can be difficult to recover. Even the state-of-the-art artifact removal methods are unable to completely remove the interference. However, desired tumor response can be easily obscured by the artifact that has a much higher order of magnitude, especially when the tumor has a relatively small size. All these pose a great challenge to the image reconstruction algorithms.

Based on the latest review study provided in [45], which evaluated seven different artifact removal methods, the best

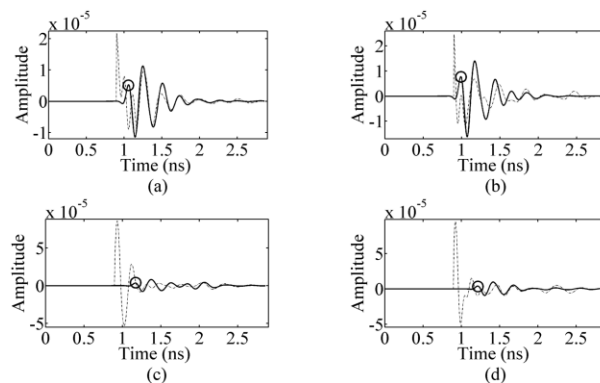


Fig. 8. (a)-(d) represent the pre-processed signals of antenna 4, 16, 33, and 46 as numbered in Fig. 1, exemplifying the performance difference between artifact removal methods. The solid and dotted curves are the results based on ideal and entropy-based method for artifact removal, respectively. The circle indicates where tumor response is expected to appear. A tumor with 10 mm diameter is placed at $(x, y, z) = (95, 99, 112)$ of the model shown in Fig. 1.

two are Wiener Filter [32] and the entropy-based time window [44]. The correlation measure between recovered tumor response by these two techniques and perfect tumor response are 0.66 and 0.60 (ranging from 0 to 1), respectively. In Wiener Filter, the artifact in each propagation channel is estimated as a filtered combination of the signals from all other channels, then the estimated artifact is subtracted from the signal received at the chosen channel. Wiener Filter can remove most of the artifact. However, this method requires the prior knowledge of the time interval in which only artifact is included. Moreover, distortion is introduced to tumor response, which might result in tumor location bias. By contrast, the entropy-based method introduces zero distortion to tumor response, has higher computational efficiency, and does not require any prior information. Hence, given both efficacy and efficiency, the entropy-based is chosen as the artifact removal method for the following study as used in [47]-[48].

Fig. 8 illustrates the entropy-based time window truncation for artifact removal. The ideal tumor response at antenna 4 is shown as the solid curve in Fig. 8(a). Comparing the actually received signal [Fig. 5(a)] with the entropy-truncated signal shown as the dotted curve in Fig. 8(a), it is noted that this method effectively removes the majority of the early-stage artifact composed of incident signals and skin-fat reflections, which has a several higher orders of magnitude than the tumor response. As shown in Fig. 5(a), the pure tumor response that has an order of magnitude of $1e-5$ is completely overwhelmed. This efficacy can also be noticed at antenna 16 [Fig. 8(b)], where almost all artifact is removed and no obvious distortion is imported, compared with the ideal tumor response within the time period from 1.0 to 1.5 (ns). However, for antenna 33 and 46 [Fig. 8(c) and (d)], there is still a large amount of residual artifact with high amplitudes. This is because in entropy-based method, the time window truncation of same length is used for signals received at all antennas [44]. Hence, depending on tumor-antenna distance variations, truncated signals of different antennas could contain varied percentages of useful tumor response versus residual artifact, which could potentially lead to location bias in constructed images.

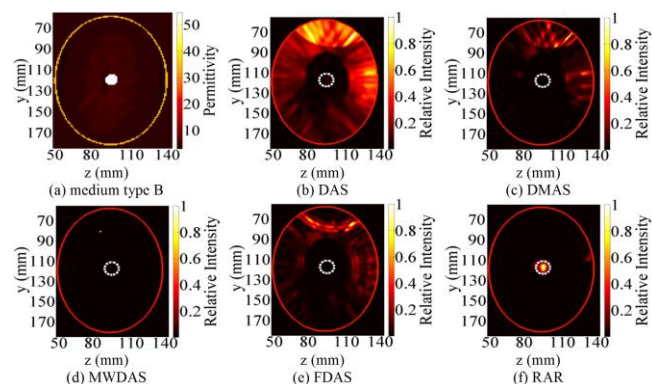


Fig. 9. (a) 2D slice of breast model with medium type B. (b)-(f) Imaging results with entropy-based artifact removal.

Fig. 9 displays the imaging results where using the same medium type B as in Fig. 7. Instead of using ideal artifact removal, the entropy-based method is applied. Compared with Fig. 7, it is noticed that the performance of DAS, DMAS, MWDAS, and FDAS suffers significantly. The result of DAS [Fig. 9(b)] is seriously unrecognizable, only an area with high intensity is observed. However, none of these high-intensity positions reveal the actual tumor location indicated by the dashed circle. Although the results of DMAS, MWDAS, and FDAS [Fig. 9(c)-(e)] only show a few focused areas, the peaks of these images are far away from the actual tumor position. In contrast, the tumor is conspicuously shown at the correct location in the image constructed by RAR [Fig. 9(f)]. This demonstrates the robust performance of RAR even if the artifact cannot be removed faultlessly. Specifically, the SCR of DAS, DMAS, MWDAS, FDAS, and RAR are -11.94 dB, -25.91 dB, -728.06 dB, -17.85 dB, and 5.27 dB, respectively. The positive SCR of RAR signifies that it is the only algorithm that reveals the tumor with correct location, which illustrates its clear advantage of excellent artifact resistance. These results also prove that effective artifact removal is vital for imaging, even for breasts with relatively low heterogeneity.

The reason behind the robustness of RAR lies in the fact that except RAR, all other algorithms simply exploit the amplitude information of time-shifted signals, expecting the maximum coherent addition or multiplication could occur at tumor locations. According to the results shown in Section IV A, this is indeed the case when tumor responses can be perfectly extracted, and all algorithms can perform well. Nevertheless, when the artifact cannot be removed effectively, it is very likely that at some non-tumor positions, only the artifact from one propagation channel can be greater than the coherent sum of tumor responses from all other channels, due to the different orders of magnitude between artifact and tumor response. For RAR, in addition to utilizing the coherent addition of tumor responses from various propagation channels, it also explores the phase coherence between signals. The introduced adaptive weight control mechanism of RAR ensures its robustness on two aspects. First, the neighborhood pairwise correlation between all antennas measures the average coherence, which is less likely to be distorted by one or two artifact signals with abnormally large amplitudes. This

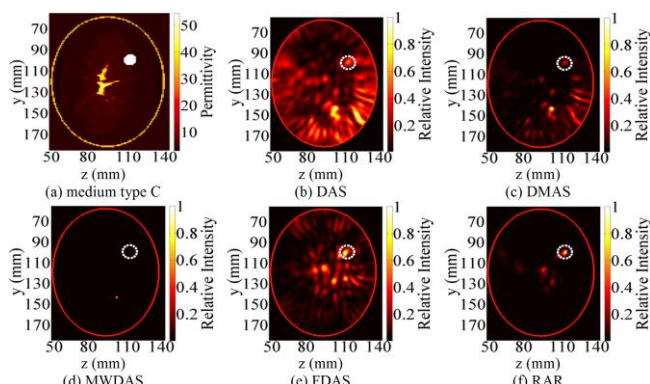


Fig. 10. (a) 2D slice of breast model with medium type C. (b)-(f) Imaging results with ideal artifact removal.

is because phase coherence is independent of signal amplitude, only the linear relationship between signal shapes affects correlation coefficients. Second, the maximum combining of pairwise coefficients adaptively focuses on those points with large scattered energy. Considering the relatively high magnitude of scattered energy from tumors over other tissues, this maintains the capability of RAR in terms of localizing tumors in most if not all cases with a much higher chance.

Aside from artifact, it is agreed that the glandular tissue forms another challenge for tumor detection. This is not only due to the substantial amount of attenuation and dispersion to received signals introduced by glandular tissues, the small dielectric contrast between cancerous and glandular tissue could easily result in misidentification of glandular tissues as tumors. Thus, it is important to evaluate algorithm's performance in such cases. Results shown in Fig. 10 are based on the collected signals from breast model with medium type C, with the same ideal artifact removal used as in [29]. Results reveal that the presence of glandular tissue can seriously deteriorate algorithms' performance, even assuming the early-stage artifact is ideally removed. Compared Fig. 10(b) with Fig. 7(b), both using the ideal artifact removal, it is observed that DAS failed to correctly localize the tumor in Fig. 10(b) where considered glandular tissues. Although the actual tumor position has a relatively high value, the peak of the constructed image no longer corresponds to tumor's position, which was the case in Fig. 7(b). This indicates the limited detectability of DAS to separate the scattering due to glandular tissues and the scattering due to the tumor. After combining signals from all propagation channels, the multi-reflections between tumor and glandular tissues could generate a higher intensity than those reflections from tumor or glandular tissues individually, which is indicated by the peak at the lower right part of Fig. 10(b). Similar erroneous tumor locations are also offered by DMAS and MWDAS [Fig. 10(c) and (d)]. Neither of them localized the tumor correctly, which indicates their vulnerability to the interference caused by glandular tissues. Despite clutter, the result offered by FDAS [Fig. 10(e)] revealed the tumor with accurately, which shows its advantage over DAS, DMAS, and MWDAS. This confirms the efficacy of the compensation of attenuation and dispersion offered by the filtering process in FDAS. The result is consistent with its

original presentation [28], whereas the slight difference is due to the different percentages of glandular tissues contained in the breast models used. However, the best imaging result is provided by RAR [Fig. 10(f)], which not only pinpoints the tumor accurately, but also provides the best clutter rejection. RAR ensures that high weights measured by correlation coefficients are obtained at tumor positions. Because after time-shifting the same signals at neighboring antenna pairs for tumor and non-tumor positions, higher correlation is obtained between tumor responses which resulted from the same high-contrast scatterer, whereas lower correlation is expected for those signals from low-contrast heterogeneous breast tissues. Thus, signals with high weights at tumor positions generate large intensities after being combined, thereby discriminating tumor responses against glandular response. Comparing the results offered by FDAS and RAR [Fig. 10(e) and (f)], although both identified the tumor, the clutter suppression capability varies considerably, and an improvement of SCR with 3.51 dB is offered by RAR. This is non-trivial, because the much more cleaner image offered by RAR can remarkably reduce the uncertainty of the existence of multi-tumors that are located near this region, which is greatly desirable in practice.

Undoubtedly, it is not realistic to assume the early-stage artifact could be ideally removed, especially considering the enormous impact of artifact, which has been confirmed in Fig. 9. Therefore, combining the entropy-based artifact removal method, the algorithm performance for heterogeneous breast models with medium type C is investigated and results are shown in Fig. 11 (Figs. 11-18 are available in supplemental materials.). In this challenging scenario, the proposed RAR is the only algorithm reveals the tumor with correct location [Fig. 11(f)], whereas with other four techniques, the tumor is either unidentifiable or with wrong estimated locations [Fig. 11(b)-(e)]. Similar to results in Fig. 9, when the early-stage artifact cannot be effectively removed, the late-stage signals no matter tumor or glandular tissue response is totally masked by the residual artifact, because of the distinctively different order of magnitudes. Even the filtering process introduced in FDAS is unable to be immune to this interference. This can be clearly illustrated by comparing Fig. 10(e) and Fig. 11(e), where ideal and entropy-based artifact removal methods are applied, respectively. These results once again confirm RAR's superiority over other methods in terms of both strong artifact resistance, and high detectability of distinguishing the scattering from tumor and glandular tissues.

Since a high percentage of breast cancers are invasive ductal carcinomas, which start at fibro-glandular regions [36], it is worth testing the imaging algorithms in the case considering tumors are very close to or grow from the glandular tissues. Fig. 12 shows a tumor located very close to glandular tissues. In the analysis of this case, the backscattered response from tumor and glandular tissues could easily overlap due to the small spacing, raising a challenge about the specificity of algorithms. Encouragingly, although with a decrease of SCR from 4.10 dB to 3.92 dB with respect to Fig. 11(f), RAR was still able to localize the tumor correctly [Fig.

12(f)]. The other four algorithms failed to do so, this proves the effectiveness of RAR for cases of ductal carcinoma.

Thus far, breasts with homogenous and inhomogeneous structures and tumors at different locations have been considered. The breast models employed before are assumed to be mildly dense, in which the fibro-glandular tissue is less than 25%. It should be considered that the increased glandular tissues could noticeably increase the breast density and result in further signal attenuation. Therefore, for comprehensive analysis, moderately and severely dense breasts are used to test algorithms in the following scenarios. In Fig. 13, the breast with medium type D is used. Although the percentage of glandular tissues for this type is normally between 25%-50%, which belongs to a moderately dense category, the randomly scattered glandular tissues can seriously reduce the homogeneity of propagation channels, making the detection of tumors much more difficult. From the results shown in Fig. 13, it is clear that RAR is again the only method that identified the tumor correctly. However, strong scattered clutters are generated. Specifically, comparing Fig. 12(f) with Fig. 13(f), the SCR of RAR results dramatically decreased from 3.92 dB to 0.48 dB. This indicates that the increased glandular tissues not only cause the change of breast density and corresponding signal attenuation, it also complicate the propagation channels, rendering the identification of strong scatterers such as tumors more difficult to be achieved. Results in Fig. 14 employed the same breast model as in Fig. 13, but the tumor is moved within the scattered glandular tissues to simulate the invasive ductal carcinoma. In comparison to Fig. 13, algorithm performance in scenario of Fig. 14 further degraded due to the further reduced uniformity of assumed propagation channels. Encouragingly, the proposed RAR algorithm in this case still kept its edge with a positive SCR of 0.10 dB (Table II), indicating its robustness to certain deviation between the assumed uniform propagation channels and the actual ones.

For completeness, the performance of all algorithms in very dense breasts with medium type E and F are also investigated. In Fig. 15, a tumor in breast model with medium type E, which includes glandular tissues with percentage ranging from 50% to 75% is considered. It is noted that the result offered by RAR algorithm [Fig. 15(f)] is the one with highest SCR of 0.05 dB, while all others have a negative SCR, corresponding to a poorer performance. Although the peak in the result of RAR does not exactly correspond to the tumor position, a relatively high intensity within the circle is observed. Also the peak generated by RAR is quite close to the tumor position, and this explains why RAR has a positive SCR. However, when the breast model with medium type F is considered (Fig. 16), all algorithms failed to differentiate between the tumor and the glandular tissue, and none were able to provide images with discernable and correct tumor positions. For both scenarios considered in Fig. 15 and Fig. 16, tumors located within fatty tissues instead of within glandular tissues are also tested to simulate various clinical scenarios. The results obtained were similar, which indicated the limited detection capability of these algorithms for severely dense breasts.

The poor performance of algorithms considered for severely dense breasts with medium type E and F is mainly due to the following three reasons. 1) Dense breasts could considerably attenuate the propagated signals, resulting in very weak tumor response contained in received signals. 2) The reflected energy from other scatterers such as glandular tissues might be equivalent or even higher than that from tumors, due to the variability in adipose versus glandular tissue compositions. 3) For almost fully dielectrically heterogeneous ACR-III and ACR-IV breasts, the assumed uniform propagation channel would not be able to represent the actual one, and fatal inaccuracy of time delay estimation could occur, leading to incorrect localization. Specifically, when the percentage of glandular tissues is higher than a certain threshold, the average estimated time delay of each propagation path might be far from the actual ones. To solve these problems, the following potential solutions could attenuate the effect of previous problems respectively: 1) Employ multistatic instead of monostatic acquisition to collect more useful backscattered signals from the tumor. 2) Enhance the contrast between tumor and the background through increasing the relative permittivity of tumor, such as using the contrast agent described in [36]. 3) Improve the accuracy of individual propagation channel estimation. The investigation of these solutions is beyond the scope of this work.

The imaging with the RAR algorithm from different view angles is also tested for completeness. The results shown in Fig. 11 with a tumor at $(x, y, z) = (95, 99, 112)$ are selected as an example. On one hand, images are reconstructed at different x planes, where $x = 85$ mm, 95 mm, and 105 mm are selected. Results illustrated that the largest intensity occurs at plane $x = 95$ mm, corresponding to the actual tumor position, proving that RAR is able to accurately identify the plane that bears the tumor. On the other, the y and z cross-section imaging results by RAR are displayed in Fig. 17, where $y = 99$ mm and $z = 112$ mm are chosen, respectively. It is observed that the reconstructed images clearly identify the tumor in both cases, with accurate positioning and strong clutter suppression.

SCR and SMR statistics of algorithms are summarized in Table II. Based on the calculated average of all ten scenarios, the proposed RAR algorithm achieves the highest SCR of 4.08 dB and SMR of 16.51 dB, respectively, indicating its excellent performance and strong robustness. It should be noted that RAR is the only algorithm which provided a positive SCR in results shown in Fig. 11, Fig. 12, Fig. 14, and Fig. 15, proving its distinct advantage. On the other hand, MWDAS has the smallest SCR and SMR in average. In spite of its excellent clutter rejection with ideal artifact removal (Fig. 6 and Fig. 7), this efficacy suffer significantly even with a small portion of residual artifact, indicating its limitation in more practical scenarios. The second best technique is FDAS, although it is very sensitive to artifact, results show that the filtering is beneficial since in most cases it outperforms the original DAS algorithm and achieves the second high SCR of -1.68 dB and SMR of 9.17 dB. Comparing DMAS with DAS, results reveal that the pure coherence-based algorithm DMAS is not always

TABLE II
 SIGNAL-TO-CLUTTER RATIO (SCR) AND SIGNAL-TO-MEAN RATIO (SMR) OF ALGORITHMS IN DIFFERENT SCENARIOS. BEST RESULTS OF EACH CASE ARE HIGHLIGHTED IN **BOLD**

	Fig. 6	Fig. 7	Fig. 9	Fig. 10	Fig. 11	
SCR (dB)						
(b) DAS	7.01	4.98	-11.94	-2.30	-3.58	
(c) DMAS	14.92	10.82	-25.91	-4.63	-5.63	
(d) MWDAS	415.58	403.25	-728.06	-78.48	-107.49	
(e) FDAS	11.43	6.77	-17.85	1.25	-4.24	
(f) RAR	13.99	8.47	5.27	4.76	4.01	
SMR (dB)						
(b) DAS	17.22	17.03	-1.87	7.62	6.90	
(c) DMAS	20.75	20.27	-12.35	7.29	7.14	
(d) MWDAS	21.14	21.08	-705.34	-56.50	-89.97	
(e) FDAS	17.22	16.47	-2.86	11.55	8.93	
(f) RAR	20.98	20.67	20.09	17.12	14.29	
	Fig. 12	Fig. 13	Fig. 14	Fig. 15	Fig. 16	Ave
SCR (dB)						
(b) DAS	-6.5	-1.83	-2.46	-0.65	-2.80	-2.00
(c) DMAS	-12.28	-0.49	-4.57	-2.35	-5.28	-3.54
(d) MWDAS	-306.46	-40.11	-87.19	-17.86	-129.46	-67.63
(e) FDAS	-11.89	0.09	-1.60	-0.31	-0.47	-1.68
(f) RAR	3.92	0.48	0.10	0.05	-0.26	4.08
SMR (dB)						
(b) DAS	2.58	9.52	7.02	9.09	5.63	8.07
(c) DMAS	-3.07	11.13	6.61	11.09	5.48	7.43
(d) MWDAS	-285.34	-61.82	-65.01	-3.34	-114.12	-133.92
(e) FDAS	1.12	10.71	9.24	10.97	8.30	9.17
(f) RAR	18.16	11.43	15.89	17.25	9.19	16.51

superior to the classic DAS. In scenarios assuming the early-stage artifact could be perfectly removed, DMAS outperforms DAS without question (Fig. 6 and Fig. 7), however, in later scenarios considered denser breasts and non-perfect artifact removal, DAS shows more robustness than DMAS. This is because the pair multiplication used in DMAS could lead to erroneous peaks in more complicated environments with less coherence among all propagation channels.

The performance of RAR algorithm with respect to tumor size was also considered. Combining entropy-based artifact removal method, in breasts with medium type A and B, tumors as small as 5 mm in diameter were successfully identified. However, in a more dielectrically heterogeneous breast with medium type C, when the tumor size is less than 7 mm in diameter, the imaging results are quite blurry, which can hardly be used to identify the tumor. As for medium type D, the smallest tumor that were successfully recognized at different positions were 10 mm as shown in Fig. 13 and Fig. 14. Additionally, the sensitivity of RAR to the error of average dielectric permittivity estimation is examined. Coupled with entropy-based artifact removal method, in mostly fatty breasts such as medium type A and B, even when the relative error is up to 30%, only a minor reduction of SCR is observed. However, for fully heterogeneous breasts with low to medium density such as medium type C and D, when the relative error is over 5%, the resulted images can rarely localize the tumor

precisely. This reinforces the need to have an accurate average dielectric permittivity estimation. In our study, the collected signals are assumed to be noiseless; in practice, however, possible measurement errors and noise need to be considered.

C. Computational Analysis

Besides robustness, complexity of algorithms is of great importance, especially for imaging 3-D realistic breast models. In this section the time complexity of algorithms is analyzed. As described before, A sets of tumor responses are collected in monostatic case, thus A signals are needed to be processed. Let K refer to signal sampling points and α be the window length, which is smaller than K . Both K and α are much more larger than A , which determine the calculation numbers for raw and truncated signals, respectively. The number of arithmetic operations (without distinguishing between addition and multiplication) needed to calculate each pixel's intensity is analyzed. All algorithms considered need the same time-shifting process, only other different processes are compared.

To sum A time-shifted signals, DAS needs $(A - 1)K$ additions. Then the summed signal is truncated by the window length α , thus α and $(\alpha - 1)$ operations for multiplication and addition are required to obtain the energy of this signal. DAS thus has an asymptotic complexity of $O(K)$.

The first step in DMAS is generating C_A^2 sets of pairs from A signals for pair multiplication, and $[(A(A - 1)/2) - 1]K$ multiplications are required. Step 2 sums $A(A - 1)/2$ signals with K sampling points, $[(A(A - 1)/2) - 1]K$ additions are involved. The last integration within the time window requires α and $(\alpha - 1)$ operations for multiplication and addition, respectively. Ignoring small values in summed operations of all steps, DMAS has an asymptotic complexity of $O(K)$.

Unlike DAS and DMAS, MWDAS brings forward the windowing of signals, thus for each signal, only α calculations are needed. Step 1 requires $(A - 1)\alpha$ summations and one division to obtain the reference waveform. Step 2 involves weighting signals from A channels via the generated reference waveform, requiring $A\alpha$ multiplications. Step 3 is the energy calculation of weighted signals and needs $(2\alpha - 1)$ operations. Last step multiplies signal energy from all channels, where $(A - 1)$ multiplications are needed. Thus MWDAS requires $(4A\alpha - 1)$ operations in all and has a complexity of $O(\alpha)$.

Two additional parts are needed for FDAS in addition to that of DAS. First is the collection of distance-dependent reference waveforms for filter design. Second is the filtering process. Since the gathering of reference signals could be precomputed, main extra computational burden of FDAS lies in the filtering process when calculating each pixel intensity. For K sampling points, $K(NK)$ multiplications are required to implement FIR filtering in time domain, where N is the filter length. Combined with extra DAS operations and ignore small values, FDAS has a complexity of $O(K^2)$ as a result.

In RAR, the windowing of signal is brought forward, thus only α calculations is required for each signal. Step 1 involves $(A - 1)$ calculation of neighborhood pairwise correlation coefficients, which requires $6\alpha(A - 1)$ operations following (5). Then the normalization needs $2(A - 1)$ operations. Step 3

sorts $(A - 1)$ normalized correlation coefficient for the maximum combining. For a sorting algorithm with $(A - 1)$ numbers, the time complexity is up to $O(A^2)$. To generate the weighted value, which is the product of the first half number of sorted coefficients, $[(A - 1)/2] - 1$ multiplications are involved. Step 4 weights the signal and α multiplications are required. Last step calculates the energy and needs $(2\alpha - 1)$ operations. Accordingly, ignoring small values in summed operations, RAR has an asymptotic complexity of $O(\alpha)$.

Simulation results on a PC with Intel (R) Core (TM) 2 Duo CPU E7500 2.93GHz (2 CPUS) combined with Matlab R2014a software confirmed the computation overhead of algorithms. 48 signals with 1500 sampling points in each signal are processed, where a time window length of 294 is employed. Thus, $A = 48$, $K = 1500$, and $\alpha = 294$ in our simulation tests. Calculated processing time employs the mean of three replicates to reduce random errors. Fig. 18 compares the complexity and processing time to calculate a single pixel intensity of algorithms. Simulation results verified the time complexity analysis. As can be seen, the complexity is mainly determined by the number of points needed to be processed in each signal, which can be K or α in different methods. A extensively higher computation burden than other algorithms is observed in FDAS, which requires the largest processing time of 1.37 seconds, whereas this time for DAS is only 0.0003 seconds. In addition, the same linear growth is observed in DAS, DMAS, MWDAS, and RAR, whereas FDAS has an exponential tendency. This demonstrates that RAR maintains the same level of high computational efficiency, even compared with the simplest DAS algorithm.

V. CONCLUSION

A novel imaging algorithm for early breast cancer detection entitled RAR is proposed. The efficacy of RAR is verified under a number of scenarios, using FDTD-based 3-D breast models with various structures and densities.

Simulation results showed imaging algorithm performance is more sensitive to the early-stage artifact, compared with the late-stage clutter, due to the different orders of magnitude of these two types of interferences. Results with superior robustness were provided by RAR in comparison to other algorithms, including DAS, DMAS, MWDAS, and FDAS. In the four of the six challenging scenarios (Fig. 11, Fig. 12, Fig. 14, and Fig. 15), RAR was the only algorithm which clearly identified and accurately localized tumors. These scenarios considered practical artifact removal, various tumor positions, and breasts ranging from mildly to moderately density classifications. Simulations also proved the computational efficiency of RAR, which has the same asymptotic complexity as DAS, DMAS, and MWDAS algorithms. The significant improvement provided by RAR is only at the expense of negligible increased computational effort. These results show the high potential of RAR for the early-stage cancer detection in low to medium density breasts. The investigation of RAR's performance for further enhancement of tumor detection in severely dense breasts will be involved in future work.

REFERENCES

- [1] F. Bray et al, "The changing global patterns of female breast cancer incidence and mortality," *Childhood*, vol. 4, pp. 5, 2004.
- [2] A. Jemal et al, "Global cancer statistics," *CA-Cancer J. Clin.*, vol. 61, no. 2, pp. 69-90, Apr. 2011.
- [3] V. Speirs and A. M. Shaaban, "The rising incidence of male breast cancer," *Breast Cancer Res. Treat.*, vol. 115, no. 2, pp. 429-430, May 2009.
- [4] I. Schreer and J. Lüttges, "Breast cancer: early detection," *Radiologic-Pathologic Correlations from Head to Toe*, pp. 767-784: Springer, 2005.
- [5] A. Bleyer and H. G. Welch, "Effect of three decades of screening mammography on breast-cancer incidence," *N. Engl. J. Med.*, vol. 367, no. 21, pp. 1998-2005, Nov. 2012.
- [6] H. D. Cheng et al, "Automated breast cancer detection and classification using ultrasound images: A survey," *Pattern Recognition*, vol. 43, no. 1, pp. 299-317, Jan. 2010.
- [7] M. Morrow et al, "MRI for breast cancer screening, diagnosis, and treatment," *The Lancet*, vol. 378, no. 9805, pp. 1804-1811, Nov. 2011.
- [8] J. G. Elmores et al, "Screening for breast cancer," *JAMA: journal of the American Medical Association*, vol. 293, no. 10, pp. 1245-1256, 2005.
- [9] D. Saslow et al, "American Cancer Society guidelines for breast screening with MRI as an adjunct to mammography," *CA-Cancer J. Clin.*, vol. 57, no. 2, pp. 75-89, 2007.
- [10] J. G. Elmores et al, "Ten-year risk of false positive screening mammograms and clinical breast examinations," *N. Engl. J. Med.*, vol. 338, no. 16, pp. 1089-1096, Apr. 1998.
- [11] A. Poulos et al, "Breast compression in mammography: How much is enough?," *Australas. Radiol.*, vol. 47, no. 2, pp. 121-126, Jun. 2003.
- [12] D. L. Preston et al, "Radiation effects on breast cancer risk: a pooled analysis of eight cohorts," *Radiat. Res.: August 2002*, vol. 158, no. 2, pp. 220-235, Aug. 2002.
- [13] B. Bocquet et al, "Microwave radiometric imaging at 3 GHz for the exploration of breast tumors," *IEEE Trans. Microw. Theory Tech.*, vol. 38, no. 6, pp. 791-793, Jun. 1990.
- [14] F. Bardati and S. Iudicello, "Modeling the visibility of breast malignancy by a microwave radiometer," *IEEE Trans. Biomed. Eng.*, vol. 55, no. 1, pp. 214-221, Jan. 2008.
- [15] L. H. V. Wang et al, "Microwave induced acoustic imaging of biological tissues," *Rev. Sci. Instrum.*, vol. 70, no. 9, pp. 3744-3748, Sep. 1999.
- [16] S. C. Hagness et al, "Two-dimensional FDTD analysis of a pulsed microwave confocal system for breast cancer detection: fixed-focus and antenna-array sensors," *IEEE Trans. Biomed. Eng.*, vol. 45, no. 12, pp. 1470-1479, Dec. 1998.
- [17] P. M. Meaney et al, "A clinical prototype for active microwave imaging of the breast," *IEEE Trans. Microw. Theory Tech.*, vol. 48, no. 11, pp. 1841-1853, Nov. 2000.
- [18] A. E. Souvorov et al, "Two-dimensional computer analysis of a microwave flat antenna array for breast cancer tomography," *IEEE Trans. Microw. Theory Tech.*, vol. 48, no. 8, pp. 1413-1415, Aug. 2000.
- [19] A. Taflov, and S. C. Hagness, *Computational electrodynamics: The Finite-Difference Time-Domain Method, 3rd*, MA: Artech House, 2000, ch. 7-9, pp. 273-406.
- [20] X. Li and S. C. Hagness, "A confocal microwave imaging algorithm for breast cancer detection," *IEEE Microw. Wireless Compon. Lett.*, vol. 11, no. 3, pp. 130-132, Mar. 2001.
- [21] E. C. Fear et al, "Confocal microwave imaging for breast cancer detection: localization of tumors in three dimensions," *IEEE Trans. Biomed. Eng.*, vol. 49, no. 8, pp. 812-822, Aug. 2002.
- [22] Y. Xie et al, "Multistatic adaptive microwave imaging for early breast cancer detection" *IEEE Trans. Biomed. Eng.*, vol. 53, no. 8, pp. 1647-1657, Aug. 2006.
- [23] Y. F. Chen et al, "Multiple-input multiple-output radar for lesion classification in ultrawideband breast imaging," *IEEE J. Sel. Topics Signal Process.*, vol. 4, no. 1, pp. 187-201, Feb. 2010.
- [24] E. A. Marengo et al, "Time-reversal MUSIC imaging of extended targets," *IEEE Trans. Image Process.*, vol. 16, no. 8, pp. 1967-1984, Aug. 2007.
- [25] M. D. Hossain et al, "Beam-space time-reversal microwave imaging for breast cancer detection," *IEEE Antennas Wireless Propag. Lett.*, vol. 12, pp. 241-244, Feb. 2013.
- [26] H. B. Lim et al, "Confocal microwave imaging for breast cancer detection: delay-multiply-and-sum image reconstruction algorithm," *IEEE Trans. Biomed. Eng.*, vol. 55, no. 6, pp. 1697-1704, Jun. 2008.
- [27] F. Yang and A. S. Mohan, "Detection of malignant breast tissues using microwave imaging," *APMC: 2009 Asia Pacific Microwave Conference, IEEE*, pp. 397-400, Dec. 2009.
- [28] A. Shahzad et al, "Prefiltered beamforming for early-stage breast cancer detection," *IEEE Antennas Wireless Propag. Lett.*, vol. 12, pp. 500-503, Apr. 2013.
- [29] A. Shahzad et al, "A Preprocessing Filter for Multistatic Microwave Breast Imaging for Enhanced Tumour Detection," *Prog. Electromagn. Res. B*, vol. 57, pp. 115-126, 2014.
- [30] University of Wisconsin Computational Electromagnetics Laboratory, Madison, WI, USA, "UWCEM numerical breast phantoms repository," 2012 [Online]. <http://uwcem.ece.wisc.edu/MRIDatabase/index.html>
- [31] M. Lazebnik et al, "A large-scale study of the ultrawideband microwave dielectric properties of normal, benign and malignant breast tissues obtained from cancer surgeries," *Phys. Med. Biol.*, vol. 52, pp. 6093-6115, 2007.
- [32] E. J. Bond et al, "Microwave imaging via space-time beamforming for early detection of breast cancer," *IEEE Trans. Antennas Propag.*, vol. 51, no. 8, pp. 1690-1705, Aug. 2003.
- [33] M. Okoniewski et al, "Simple treatment of multi-term dispersion in FDTD," *IEEE Microw. Guided Wave Lett.*, vol. 7, pp. 121-123, May 1997.
- [34] E. Zastrow et al, "Development of anatomically realistic numerical breast phantoms with accurate dielectric properties for modeling microwave interactions with the human breast," *IEEE Trans. Biomed. Eng.*, vol. 55, no. 12, pp. 2792-2800, Dec. 2008.
- [35] American College of Radiology, *Breast Imaging Reporting and Data System (BI-RADS) Atlas*, 4th ed. Reston, VA: Amer. Coll. Radiol., 2003.
- [36] Y. Chen et al, "Feasibility study of lesion classification via contrast-agent-aided UWB breast imaging," *IEEE Trans. Biomed. Eng.*, vol. 57, no. 5, pp. 1003-1007, May 2010.
- [37] J. A. LaComb et al, "Ultra wideband surface wave communication," *Prog. Electromagn. Res. C*, vol. 8, pp. 95-105, 2009.
- [38] P. Dimbylow, "FDTD calculations of the whole-body averaged SAR in an anatomically realistic voxel model of the human body from 1 MHz to 1 GHz," *Phys. Med. Biol.*, vol. 42, no. 3, pp. 479, Mar. 1997.
- [39] J. A. Roden and Stephen D. Gedney, "Convolutional PML (CPML): An efficient FDTD implementation of the CFS-PML for arbitrary media," *Microw. Opt. Technol. Letters*, vol. 27, no. 5, pp. 334-338, 2000.
- [40] J. M. Sill and E. C. Fear, "Tissue sensing adaptive radar for breast cancer detection-experimental investigation of simple tumor models," *IEEE Trans. Microw. Theory Techn.*, vol. 53, no. 11, pp. 3312-3319, Nov. 2005.
- [41] P. K. Verma et al, "Analysis of clutter reduction techniques for through wall imaging in UWB range," *Prog. Electromagn. Res. B*, vol. 17, pp. 29-48, 2009.
- [42] M. Klemm et al, "Improved delay-and-sum beamforming algorithm for breast cancer detection," *Int. J. of Antennas Propag.*, 2008.
- [43] A. Maskooki et al, "Frequency domain skin artifact removal method for ultra-wideband breast cancer detection," *Prog. Electromagn. Res.*, vol. 98, pp. 299-314, 2009.
- [44] W. Zhi and F. Chin, "Entropy-based time window for artifact removal in UWB imaging of breast cancer detection," *IEEE Signal Process. Lett.*, vol. 13, no. 10, pp. 585-588, Oct. 2006.
- [45] M. A. Elahi et al, "Artifact removal algorithms for microwave imaging of the breast," *Prog. Electromagn. Res.*, vol. 141, pp. 185-200, 2013.
- [46] D. Winters et al, "Estimation of the frequency-dependent average dielectric properties of breast tissue using a time-domain inverse scattering technique," *IEEE Trans. Antennas Propag.*, vol. 54, no. 11, pp. 3517-3528, Nov. 2006.
- [47] M. D. Hossain and A. S. Mohan, "Breast cancer detection in highly dense numerical breast phantoms using time reversal," *Electromagnetics in Advanced Applications (ICEAA), 2013 International Conference on IEEE*, pp. 859-862, Sep. 2013.
- [48] M. D. Hossain and A. S. Mohan, "Beam-space time reversal maximum likelihood estimation for microwave breast imaging," *Antennas and Propagation Society International Symposium, 2014*, pp. 1921-1922, Jul. 2014.